Title

HOPS-dependent endosomal fusion required for efficient cytosolic delivery of therapeutic peptides and small proteins

Journal

Proceedings of the National Academy of Sciences of the United States of America, 116(2)

ISSN

0027-8424

Authors

Steinauer, Angela
LaRochelle, Jonathan R
Knox, Susan L
et al.

Publication Date

2019-01-08

DOI

10.1073/pnas.1812044116

Peer reviewed

HOPS-dependent endosomal fusion required for efficient cytosolic delivery of therapeutic peptides and small proteins

Angela Steinauer[a], Jonathan R. LaRochelle[b], Susan L. Knox[a], Rebecca F. Wissner[a], Samuel Berry[c], and Alanna Schepartz[a,b,1]

[a]Department of Chemistry, Yale University, New Haven, CT 06520-8107; [b]Department of Molecular, Cellular and Developmental Biology, Yale University, New Haven, CT 06520-8103; and [c]Department of Molecular Biophysics and Biochemistry, Yale University, New Haven, CT 06520-8114

Edited by James A. Wells, University of California, San Francisco, CA, and approved November 26, 2018 (received for review July 17, 2018)

Protein therapeutics represent a significant and growing component of the modern pharmacopeia, but their potential to treat human disease is limited because most proteins fail to traffic across biological membranes. Recently, we discovered a class of cell-permeant miniature proteins (CPMPs) containing a precisely defined, penta-arginine (penta-Arg) motif that traffics readily to the cytosol and nucleus of mammalian cells with efficiencies that rival those of hydrocarbon-stapled peptides active in animals and man. Like many cell-penetrating peptides (CPPs), CPMPs enter the endocytic pathway; the difference is that CPMPs containing a penta-Arg motif are released efficiently from endosomes, while other CPPs are not. Here, we seek to understand how CPMPs traffic from endosomes into the cytosol and what factors contribute to the efficiency of endosomal release. First, using two complementary cell-based assays, we exclude endosomal rupture as the primary means of endosomal escape. Next, using an RNA interference screen, fluorescence correlation spectroscopy, and confocal imaging, we identify *VPS39*—a gene encoding a subunit of the homotypic fusion and protein-sorting (HOPS) complex—as a critical determinant in the trafficking of CPMPs and hydrocarbon-stapled peptides to the cytosol. Although CPMPs neither inhibit nor activate HOPS function, HOPS activity is essential to efficiently deliver CPMPs to the cytosol. CPMPs localize within the lumen of Rab7$^+$ and Lamp1$^+$ endosomes and their transport requires HOPS activity. Overall, our results identify Lamp1$^+$ late endosomes and lysosomes as portals for passing proteins into the cytosol and suggest that this environment is prerequisite for endosomal escape.

cell-penetrating peptides | peptidomimetics | enzyme replacement therapy | endocytosis | protein therapeutics

Protein and peptide therapeutics—biologics—comprise a rapidly growing sector of the modern pharmacopeia (1). Seven of the top 10 highest grossing therapeutic agents in 2017 were biologics used to treat cancer, diabetes, and autoimmune inflammatory disorders, such as rheumatoid arthritis and Crohn's disease. In each case, the biologic acts by stimulating, inhibiting, or replacing a protein located within plasma or on an external membrane surface. Not one acts within the cell cytosol or nucleus, in large part because most proteins cannot effectively breach the barrier defined by the plasma membrane (2). The well-known early exceptions to this rule discovered by Green and Loewenstein (3), Frankel and Pabo (4), and Derossi et al. (5)—the HIV transactivator of transcription (Tat) protein and the Antennapedia homeodomain—have inspired the synthesis, study, and (in some cases) clinical evaluation (6) of hundreds of arginine-rich cell-penetrating peptides (CPPs) (7). The problem is that when added to cells, most CPPs remain trapped in endosomes and fail to achieve significant concentrations in the cytosol or nucleus (8). The inefficient delivery of proteins, peptides, and their mimetics into the mammalian cell cytosol limits their potential as therapeutics and research tools.

Recently, we discovered that, when added to cells, certain small, folded miniature proteins (9, 10) derived from avian pancreatic polypeptide (aPP) or an isolated zinc-finger (ZF) domain, are taken up into the endocytic pathway and subsequently released into the cytosol with unprecedented efficiencies (11, 12). The most effective molecules are defined by a discrete array of five arginine residues on a folded α-helix (13); we refer to these molecules as cell-permeant miniature proteins (CPMPs). Treatment of HeLa cells in culture with the CPMP ZF5.3 leads to a ZF5.3 concentration in the cytosol that is roughly 67% of the extracellular incubation concentration; this value is at least 10-fold higher than that achieved by the HIV-Tat$_{48–60}$ peptide (14) or octaarginine (Arg8) and equal to that of hydrocarbon-stapled peptides under development as protein–protein interaction inhibitors (15). Improvements in cytosolic access between two- and sixfold are observed when the CPMP ZF5.3 is fused to protein cargos with significant molecular mass (16).

Here, we describe experiments that seek to understand how CPMPs like ZF5.3 traffic from endosomes into the cytosol, and what factors contribute to the efficiency of endosomal release. First, using two complementary cell-based assays, we exclude endosomal rupture as the primary means of endosomal escape.

Significance

The potential of protein therapeutics is limited because most proteins cannot reach the cytosol. Like many cell-penetrating peptides (CPPs), cell-permeant miniature proteins (CPMPs) that embody a penta-Arg motif are endocytosed; the difference is that CPMPs are released efficiently from endosomes while other CPPs are not. Here, we report that the trafficking of CPMPs into the cytosol requires the homotypic fusion and protein-sorting (HOPS) complex, a membrane-tethering complex that fuses Rab7$^+$ endosomes. CPMPs neither inhibit nor activate HOPS function; instead, HOPS allows CPMPs to traffic into Lamp1$^+$ endosomes as a prerequisite for endosomal escape. The identification of Lamp1$^+$ late endosomes and lysosomes as portals for passing proteins into the cytosol will aid the development of next-generation biologics that overcome the limitations imposed by cellular membranes.

Author contributions: A. Steinauer, J.R.L., R.F.W., and A. Schepartz designed research; A. Steinauer, J.R.L., S.L.K., R.F.W., and S.B. performed research; A. Steinauer, J.R.L., S.L.K., R.F.W., and A. Schepartz analyzed data; and A. Steinauer, J.R.L., R.F.W., and A. Schepartz wrote the paper.

Conflict of interest statement: A. Schepartz. and R.F.W. are named inventors of pending patent applications related to the work described.

This article is a PNAS Direct Submission.

[1]To whom correspondence should be addressed. Email: alanna.schepartz@yale.edu.

This article contains supporting information online at www.pnas.org/lookup/suppl/doi:10.1073/pnas.1812044116/-/DCSupplemental.

Published online January 4, 2019.

Next, using an RNA interference (RNAi) screen, fluorescence correlation spectroscopy (FCS), and confocal imaging, we identify *VPS39*—a gene encoding a subunit of the homotypic fusion and protein-sorting (HOPS) complex—as a critical determinant in the trafficking of CPMPs and hydrocarbon-stapled peptides to the cytosol. HOPS activity is essential for cytosolic access; the closely related class C core vacuole/endosome tethering (CORVET) complex is not required. Although CPMPs neither inhibit nor activate HOPS function, HOPS activity is required to efficiently deliver CPMPs to the cytosol. Multicolor confocal imaging studies identify CPMPs within the lumen of $Rab7^+$ and $Lamp1^+$ endosomes and their transport to $Lamp1^+$ endosomes requires HOPS activity. Within these compartments, CPMPs associate with intraluminal vesicles (ILVs). We conclude that HOPS is essential because it allows CPMPs to traffic into ILV-containing $Rab7^+$ and $Lamp1^+$ endosomes, where they encounter a favorable environment for endosomal escape.

Results

Evaluating Endosomal Damage. Partial or full endosomal rupture (17) is one pathway by which a CPMP could reach the cytosol or nucleus, yet the concentration-dependent effects of CPMPs or more traditional CPPs on endosomal integrity in cultured cells have not been thoroughly evaluated. We developed two complementary assays that together detect both subtle and severe endosomal damage in cells treated with a CPMP or CPP. One exploits eGFP-labeled galectins (Gal) to fluorescently tag damaged endosomes to enable their visualization using confocal microscopy, while the other employs a fluorescently tagged version of the nonalysine (Lys9) peptide to quantify the extent of endosome rupture in cells treated with a CPMP or CPP. In both cases, the effects of CPMPs—aPP5.3 (**1**) and ZF5.3 (**2**)—were compared with those of prototypic members of three CPP families: the hydrocarbon-stapled peptide SAH-p53-8 (**3**) (15); D-octaarginine (D-Arg8, **4**) (18), and a cyclic peptide containing both natural and unnatural amino acids, CPP12 (**5**) (19) (Fig. 1 and *SI Appendix*, Fig. S1). SAH-p53-8 (**3**) is a hydrocarbon-stapled peptide that reaches the cell interior despite the absence of excess positive charge, D-Arg8 (**4**) is the proteolytically stable enantiomer of the widely studied octapeptide L-Arg8 (18), and CPP12 (**5**) is a cyclic peptide that reportedly reaches the cytosol with an efficiency that rivals aPP5.3 (19).

CPMPs and CPPs Do Not Induce Gal Recruitment at Submicromolar Concentrations. A characteristic feature of damaged endosomes (20–26) is the presence of cytosolic β-galactosides that are ordinarily found on the luminal side of endolysosomal compartments (27).

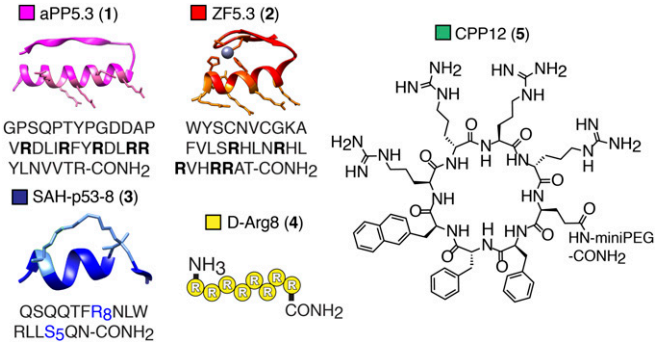

Fig. 1. CPMPs and CPPs evaluated herein include aPP5.3 (**1**) (model structure from PDB ID code 1PPT); ZF5.3 (**2**) (model structure from PDB ID code 2EOZ); SAH-p53-8 (**3**) (model structure from PDB ID code 3V3B); D-Arg8 (**4**); and the cyclic peptide CPP12 (**5**). Unnatural amino acids: R_8, *R*-octenylalanine; S_5, *S*-pentenylalanine. See also *SI Appendix*, Fig. S1 and Table S1.

These β-galactosides recruit cytosolic Gal proteins (28, 29) that share a conserved β-galactoside binding site (*SI Appendix*, Fig. S2*A*) (30, 31). In particular, Gal3 and Gal8 are recruited to damaged $Rab7^+$ and $Lamp1^+$ endosomes that form along the degradative branch of the endocytic pathway (20, 31). Previous work has shown that endosomal damage can be detected by monitoring the translocation of eGFP fusions of Gal3 or Gal8 from the cytosol to endosome surfaces (20–26). However, the effects of CPPs or CPMPs on the extent of Gal-recruitment to potentially damaged endosomes have not previously been studied.

To evaluate whether CPMPs, such as aPP5.3 (**1**) and ZF5.3 (**2**), lead to the recruitment of Gal to endosomal compartments, we made use of eGFP fusions of human Gal3 (eGFP-hGal3) and human Gal8 (eGFP-hGal8), both of which have been used previously to detect endosomal damage (22, 30, 31). Human osteosarcoma (Saos-2) cells transiently expressing eGFP-hGal3 or eGFP-hGal8 were first treated for 1 h with two known endosomolytic agents at concentrations reported to induce endosomal rupture and then imaged using confocal microscopy to assess the level of Gal recruitment from the cytosol to damaged endosomes (*SI Appendix*, Fig. S2*B*). The two endosomolytic agents used as positive controls were Lipofectamine RNAiMAX (31, 32) (referred to as RNAiMAX henceforth; 16 μL/mL) and L-leucyl-L-leucine methyl ester (LLOMe; 1 mM) (22). The extent of endosomal recruitment was quantified using ImageJ (33) by calculating an endosomal recruitment coefficient (ERC), which was defined as the percent-area of punctate fluorescence observed in a single cell divided by the total cell area, multiplied by 100 (*SI Appendix*, Fig. S2*C*). As expected (27, 31), expression of eGFP-hGal3 or eGFP-hGal8 in untreated Saos-2 cells led to uniform eGFP fluorescence throughout the cytosol and nucleus with negligible punctate staining (*SI Appendix*, Fig. S2*B*). The average ERC values calculated in untreated Saos-2 cells expressing eGFP-hGal3 or eGFP-hGal8 were 2.0 ± 0.6 and 3.4 ± 0.7, respectively (*SI Appendix*, Fig. S2*D*). In contrast, treatment of Saos-2 cells with either RNAiMAX or LLOMe, both of which stimulate Gal3 and Gal8 recruitment to endolysosomal membranes in multiple cell lines (20, 22, 30, 31), led to significant punctate staining (*SI Appendix*, Fig. S2*B*). As previously reported, Gal recruitment occurred within minutes and persisted for several hours (30). The average ERC values calculated when Saos-2 cells were treated with RNAiMAX were 62 ± 8 (Gal-3) and 42 ± 5 (Gal-8), values that represent increases of 30- and 14-fold over untreated cells (*SI Appendix*, Fig. S2 *B* and *D*). The effects of LLOMe were even more dramatic: the average ERC values in Saos-2 cells expressing eGFP-hGal3 or eGFP-hGal8 treated with LLOMe increased 147- and 68-fold compared with untreated cells, respectively. These data confirm the utility of eGFP-hGal3 and eGFP-hGal8 for monitoring CPP- or CPMP-induced endolysosomal damage in Saos-2 cells.

We next examined the effects of CPMPs aPP5.3 (**1**) and ZF5.3 (**2**) on the endosomal recruitment of eGFP-hGal3 and eGFP-hGal8. Side-by-side experiments were performed with SAH-p53-8 (**3**), D-Arg8 (**4**), and CPP12 (**5**). Each CPMP or CPP was tagged with a lissamine rhodamine B fluorophore (R) to enable its selective visualization alongside the eGFP-fused Gal. Gal-expressing Saos-2 cells were treated with 600 nM $\mathbf{1}^R$–$\mathbf{5}^R$ (60 min), washed, and incubated for 30 min in CPMP/CPP-free media before imaging with confocal microscopy. This analysis revealed punctate red fluorescence throughout the cytosol, indicating endocytic uptake of CPMPs and CPPs $\mathbf{1}^R$–$\mathbf{5}^R$, and a uniform distribution of eGFP-hGal3 and -8 throughout the cytosol and nucleus (*SI Appendix*, Fig. S2*B*). The average ERC values calculated when Saos-2 cells expressing eGFP-hGal3 or eGFP-hGal8 were treated with 600 nM CPMPs or CPPs $\mathbf{1}^R$–$\mathbf{5}^R$ were all less than 15 (*SI Appendix*, Fig. S2*D*), which is not significantly above the ERC of untreated Saos-2 cells. These data

suggest that $\mathbf{1}^{R}$–$\mathbf{5}^{R}$ cause little or no Gal^{+} endosomal damage at a treatment concentration of 600 nM.

CPMPs and CPPs Do Not Induce Endosomal Leakage at Concentrations Below 2 μM. Although monitoring Gal recruitment reports on endolysosomal damage characterized by the cytosolic display of β-galactosides, it does not necessarily capture transient damage that can result in partial or complete endosomal leakage. To explore whether treatment of cells with CPMPs or CPPs causes endosomal leakage, we developed an assay to detect the release of lissamine rhodamine B-tagged Lys9 ($Lys9^{R}$) from endosomes into the cytosol in the presence of CPPs or CPMPs. The nonapeptide Lys9 is internalized via endocytosis but not released into the cytosol under normal physiological conditions (34, 35). We verified this finding, and then used FCS (12) to quantify the concentration of $Lys9^{R}$ that reached the cytosol in the presence of CPMPs or CPPs (*SI Appendix*, Fig. S3*A*). Control experiments confirmed that Saos-2 cells treated with increasing concentrations of RNAiMAX (0–16 μL/mL) exhibited a dose-dependent increase in $Lys9^{R}$, which was detected in the cytosol and nucleus using FCS (*SI Appendix*, Fig. S3*B*). Similar titration experiments with LLOMe yielded no detectable endosomal leakage of $Lys9^{R}$, even at the highest tested LLOMe concentration (1 mM) (*SI Appendix*, Fig. S3*C*). LLOMe selectively induces lysosomal permeabilization (36, 37); it is possible that $Lys9^{R}$ leakage can only occur efficiently from endosomes that precede the lysosome (LY), an observation that has also been made for the endosomal escape of small-interfering RNA (siRNA) lipoplexes (31) and a disulfide-bonded dimer of Tat (dfTat) (38).

Additional control experiments using FCS and fractionation confirmed that the cytosolic access of each CPMP or CPP was similar in the presence and absence of unlabeled Lys9 ($Lys9^{UL}$) (*SI Appendix*, Fig. S4*A*). As reported previously for experiments performed in HeLa cells, CPMPs $\mathbf{1}^{R}$ and $\mathbf{2}^{R}$ and the hydrocarbon-stapled peptide $\mathbf{3}^{R}$ reached the cytosol and nucleus with significantly greater efficiency than CPPs $\mathbf{4}^{R}$ and $\mathbf{5}^{R}$, although cytosolic delivery was generally about twofold lower in Saos-2 cells than in HeLa cells (12). After confirming that the presence of Lys9 had no significant effect on the ability of CPMP/CPPs $\mathbf{1}^{R}$–$\mathbf{5}^{R}$ to reach the cytosol, we evaluated the extent to which $Lys9^{R}$ leaked from endosomes into the cytosol or nucleus after treatment with an unlabeled CPMP or CPP ($\mathbf{1}^{UL}$–$\mathbf{5}^{UL}$) at concentrations between 0.3 and 2.4 μM. No significant leakage of $Lys9^{R}$ into the cytosol or nucleus was observed at CPMP or CPP concentrations below 2 μM (*SI Appendix*, Fig. S3 *D–H*). At 2.4 μM, CPMPs $\mathbf{1}^{UL}$ and $\mathbf{2}^{UL}$ induced low levels of $Lys9^{R}$ endosomal leakage (*SI Appendix*, Fig. S3 *D* and *E*), corresponding to a 6- and 10-fold increase above background for $\mathbf{1}^{UL}$ and $\mathbf{2}^{UL}$, respectively. The remaining polypeptides $\mathbf{3}^{UL}$–$\mathbf{5}^{UL}$ did not induce significant $Lys9^{R}$ leakage at any concentration tested in this assay (*SI Appendix*, Fig. S3 *F–H*). Taking these data together, we find that the Gal recruitment and Lys9 leakage assays demonstrate that CPMPs and CPPs $\mathbf{1}^{R}$–$\mathbf{5}^{R}$/$\mathbf{1}^{UL}$–$\mathbf{5}^{UL}$ do not induce endosomal rupture at concentrations below 2 μM. Above 2 μM, $\mathbf{1}^{UL}$ and $\mathbf{2}^{UL}$ induce low levels of $Lys9^{R}$ leakage, indicating that they are causing endosomal damage. Toxicity studies that monitored metabolic activity over an extended 4-h timeframe by detecting cellular ATP (CellTiter-Glo) revealed EC_{50} values for $\mathbf{1}^{UL}$, $\mathbf{2}^{UL}$, $\mathbf{4}^{UL}$, $\mathbf{5}^{UL}$ that were >20 μM; the value for SAH-p53-8, $\mathbf{3}^{UL}$, was 4.0 μM (*SI Appendix*, Fig. S4*B*).

Design of a Genome-Wide RNAi Screen to Probe Endosomal Release. The observation that submicromolar concentrations of CPMPs aPP5.3 (**1**) and ZF5.3 (**2**) can efficiently access the cytosol without significantly perturbing endosomal membranes raised the possibility that CPMP release from endosomes exploits a distinct cellular mechanism. To characterize this mechanism, we designed a genome-wide RNAi screen to identify candidate genes whose knockdown increase or decrease the ability of CPMP **1** to reach the cytosol. To quantify cytosolic delivery of **1**, we made use of a previously reported glucocorticoid-induced eGFP translocation (GIGT) assay (11, 13, 39) that couples the cytosolic delivery of a molecule tagged with dexamethasone (Dex) to the nuclear translocation of a reporter protein consisting of a glucocorticoid receptor variant with exceptional affinity for dexamethasone (GR*) (40, 41) fused to eGFP (GR*-eGFP) (*SI Appendix*, Fig. S5*A*). The effect of the Dex-tagged molecule on the ratio of GFP fluorescence in the nucleus and cytosol, termed the translocation ratio (TR), can be measured with precision using an Opera high-content screening system and thereby provides a quantifiable readout of cytosolic access (11, 13). Previously, we demonstrated that the GIGT/Opera combination assay is associated with robust *Z*-factors of ≥0.5 and is therefore suitable for quantifying the cytosolic delivery of Dex-labeled CPMPs $aPP5.3^{Dex}$ ($\mathbf{1}^{Dex}$) and $ZF5.3^{Dex}$ ($\mathbf{2}^{Dex}$) in a high-throughput setting (13). Saos-2 cells stably expressing GR*-GFP [Saos-2(GIGT) cells] were prepared as described previously (13).

Before conducting the RNAi screen in a genome-wide format, we optimized cell density and siRNA transfection conditions to integrate the GIGT assay with high-content RNAi screening in Saos-2(GIGT) cells (*SI Appendix*, Fig. S5*B*). We then performed a duplicate pilot screen with 320 randomly chosen siRNAs from the Dharmacon human genome library. With this subset of siRNAs, we assessed assay performance in Saos-2(GIGT) cells treated with the CPMP $\mathbf{1}^{Dex}$ at 1-μM concentration, which yielded the highest signal-to-background (S/B) ratio (*SI Appendix*, Fig. S5*C*). Performance was robust across this siRNA test panel, with a mean S/B ratio of 2.3 when comparing the TR of Saos-2(GIGT) cells treated with $\mathbf{1}^{Dex}$ to untreated cells; the S/B ratio of an average siRNA screen is 2.9 (42). The observed coefficient of variation, a measure of data variability, was also excellent; the 11.2% value observed was below the average observed in both small-molecule and siRNA screens (42). The calculated *Z*-factor (*Z′*) was 0.3, within the acceptable range for siRNA screens (42), and the reproducibility between replicate wells was high (Pearson correlation coefficient: $r = 0.8$) (*SI Appendix*, Fig. S5*C*). Collectively, these statistics are modestly better than the average of representative RNAi screens (42) and highlight the suitability of the GIGT/Opera combination assay for high-content RNAi screening.

We then used the GIGT/Opera combination assay to evaluate the effects of siRNAs targeting the majority (18,118) of human genes on the cytosolic localization of $aPP5.3^{Dex}$ ($\mathbf{1}^{Dex}$). Saos-2 (GIGT) cells were transfected in triplicate for 72 h with pools of four siRNAs targeting different regions of the same human mRNA, serum-starved overnight, and treated with 1 μM $\mathbf{1}^{Dex}$ for 30 min (*SI Appendix*, Fig. S5*D*). The cells were fixed, nuclei were stained, and the relative amounts of GR*-eGFP in the cytosol and nucleus quantified to generate a TR. The raw TR of each experimental well was converted to a normalized percent effect value (*SI Appendix*, Eq. **S10**). The average TR of Saos-2(GIGT) cells transfected with a nontargeting siRNA (RISC-free) and treated with 1 μM $\mathbf{1}^{Dex}$ was defined as 0% effect, while that of Saos-2(GIGT) cells without $\mathbf{1}^{Dex}$ transfected with nontargeting siRNA was defined as 100% effect.

Hit Identification and Initial Prioritization. Hits were identified from the data set by applying a strictly standardized mean difference (SSMD, β) threshold of 2.0 (43). This SSMD threshold identified 428 candidate genes that altered the GR*-eGFP translocation in the presence of $\mathbf{1}^{Dex}$ across three replicates (*SI Appendix*, Fig. S5 *D* and *E*). The set of 428 candidate genes consisted of 165 genes whose knockdown inhibited and 263 genes whose knockdown enhanced GR*-eGFP translocation with $\mathbf{1}^{Dex}$ (Dataset S1). Genes whose knockdown inhibited GR*-eGFP translocation in

the presence of $\mathbf{1}^{Dex}$ displayed average percent effect values between −26 and −100% (average = −44 ± 10%) compared with positive control cells treated with a nontargeting siRNA and $\mathbf{1}^{Dex}$ (*SI Appendix*, Fig. S5*E*, siRNA hit type 1). Genes whose knockdown increased GR*-eGFP translocation displayed average percent effect values between +50 and +250% (average = +96 ± 29%) higher than controls (*SI Appendix*, Fig. S5*E*, siRNA hit type 2). Genes whose knockdown failed to alter the GR*-eGFP translocation induced by $\mathbf{1}^{Dex}$ displayed mean percent effect values that remained unchanged compared with control cells (*SI Appendix*, Fig. S5*E*, no siRNA effect). The primary hit rate of 2.4% (*SI Appendix*, Fig. S5*F*) falls within the range typically observed during cell-based RNAi screens (median primary hit rate of 2.3%) (44) and reflects the conservative nature of the SSMD value used for thresholding hits from the primary screen. While genes implicated in endocytosis (45) were enriched among the set of 428 initial hits (102 genes, 24% of the total), a protein–protein interaction analysis using the String database (46) revealed many interactions but no singular enriched mechanism or pathway.

To focus our attention on genes involved in the endosomal release of CPMP $\mathbf{1}^{Dex}$, we prioritized the set of 428 initial hits to focus on genes of unknown function (29 genes) and those implicated previously in endocytic trafficking (102 genes) (Dataset S2). Unknown genes were identified using the publicly available GeneCards and Rat Genome Database databases (47, 48). Genes implicated in endocytic trafficking were identified using a previously reported systems-level survey of endocytosis (45). The 297 genes lost in this filtering step encompass diverse functions. To confirm that we had successfully prioritized genes of unknown function and those implicated previously in endocytic trafficking, we cross-referenced the set of 131 prioritized genes with the Database for Annotation, Visualization and Integrated Discovery (DAVID) (49, 50). We specified the gene ontology classification "cellular compartment" to evaluate the "enrichment" of this set of 131 genes with respect to categories of subcellular organelles. The most enriched organelle categories, according to the database analysis, were the Golgi stack, the LY membrane, and the late endosome (LE). This analysis provides confidence that the set of 131 prioritized genes were worthy of subsequent study.

We recognized that some of the remaining siRNAs could be associated with the GR signaling pathway and affect the cytosolic to nuclear distribution of GR*-eGFP even in the absence of Dex or $\mathbf{1}^{Dex}$. To identify these genes, we evaluated the individual effect of each of the four gene-specific siRNAs targeting the remaining 131 candidate genes on the distribution of GR*-GFP in nontreated Saos-2(GIGT) cells. We discarded a gene if three of the four gene-specific siRNAs significantly increased the TR compared with that measured in Saos-2(GIGT) cells transfected with a nontargeting siRNA in the absence of Dex or a Dex-labeled peptide, indicating that the gene knockdown primarily affects GR*-GFP distribution independent of the cytosolic presence of Dex or a Dex-labeled peptide. This process eliminated 61 genes from consideration (Dataset S3), leaving 70 genes for subsequent validation.

Next, focusing on these remaining 70 genes, we evaluated the individual effect of each of the four gene-specific siRNAs on the TR measured in Saos-2(GIGT) cells treated with either CPMP $\mathbf{1}^{Dex}$ or $\mathbf{2}^{Dex}$, which both carry the discrete arginine array that exemplifies a penta-arginine (penta-Arg) motif. We reasoned that this siRNA deconvolution procedure would identify those genes involved in cellular trafficking of both $\mathbf{1}^{Dex}$ and $\mathbf{2}^{Dex}$, and simultaneously minimize false-positives that result from siRNA off-target effects (51). Genes were retained if at least two of the four siRNAs in the pool led to significant TR changes (by one-way ANOVA test with Dunnett post hoc test) in the presence of either $\mathbf{1}^{Dex}$ or $\mathbf{2}^{Dex}$ compared with that observed in Saos-2 (GIGT) cells transfected with a nontargeting siRNA; 28 of the 70 candidate genes passed this filter (Dataset S4). This final set of 28 genes displayed significant enrichment for membrane compartments (19 of 28 genes) when specifying the gene ontology term "cellular compartments," but did not exhibit enriched protein–protein interaction networks (46).

Prioritizing Hits Based on Mechanism: Genetic Knockdowns That Selectively Mediate Endosomal Escape. Although the GIGT/Opera combination assay is useful for analyzing the effect on siRNA knockdowns on cytosolic access in a high-throughput mode, it is inherently qualitative and does not differentiate between knockdowns that alter CPMP/CPP uptake from those that only affect endosomal escape. To further validate and differentiate between the remaining 28 candidate genes on the basis of these criteria, we turned to two quantitative methods: flow cytometry (FC) and FCS (12). When used together, FC and FCS effectively discriminate knockdowns that alter overall CPMP/CPP uptake (quantified by FC) from those that affect endosomal escape (quantified by FCS). To evaluate the effects of each siRNA knockdown on the trafficking of CPMPs using FC and FCS, we chose to focus on CPMP $\mathbf{2}^{R}$; while CPMPs $\mathbf{1}^{R}$ and $\mathbf{2}^{R}$ follow a similar endocytic trafficking pattern into the cell interior (11), $\mathbf{2}^{R}$ is more stable and reaches the cytosol more efficiently (12).

To evaluate the effect of the 28 candidate genes on CPMP uptake and endosomal release, Saos-2 cells were treated with pooled gene-specific siRNAs for 72 h. Transfected Saos-2 cells were then treated with 600 nM $\mathbf{2}^{R}$ for 30 min, lifted with trypsin to remove plasma membrane-bound peptide (11), and analyzed using FC and FCS to quantify both overall cellular uptake and the concentration of $\mathbf{2}^{R}$ that reached the cell interior. Real-time quantitative PCR (RT-qPCR) experiments confirmed that the knockdown efficiency of each siRNA pool was >70% in Saos-2 cells (*SI Appendix*, Fig. S6*A*). Additional control experiments confirmed that neither RNAiMAX nor knockdown of the housekeeping gene *GAPD* affected overall CPMP uptake by Saos-2 cells (as determined by FC) or intracellular delivery of $\mathbf{2}^{R}$ (as determined by FCS) (*SI Appendix*, Fig. S6*B*).

Knockdown of the 28 candidate genes led to significant differences in the overall uptake and intracellular delivery of $\mathbf{2}^{R}$. Knockdown of only 4 of the 28 candidate genes (*VPS39*, *SCAMP5*, *PIGW*, and *DOCK4*) significantly decreased the overall uptake of $\mathbf{2}^{R}$, as determined using FC (Fig. 2*A*); none of the siRNAs significantly increased overall uptake when measured in this way. Different trends emerged when siRNA knockdown effects were evaluated using FCS (Fig. 2 *B* and *C*); in this case, 19 of 28 knockdowns led to a significant decrease in the concentration of $\mathbf{2}^{R}$ in the cytosol or nucleus. Knockdown of 6 of the 28 candidate genes strongly reduced (>70%) the delivery of $\mathbf{2}^{R}$ to the nucleus and cytosol: these genes include *VPS39*, *SCAMP5*, *PXN*, *PIGW*, *MS4A4A*, and *LYPLA1* (Fig. 2 *B* and *C*). Knockdown of an additional 13 candidate genes moderately reduced (40–70%) the delivery of $\mathbf{2}^{R}$ to the nucleus and cytosol: these genes include *TAS2R45*, *CASC1*, *KLHDC10*, *CSGALNACT2*, *INA*, *IL17REL*, *RAB2A*, *ZYX*, *INADL*, *ABPA3*, *GNG13*, *AVL9*, and *TVP23A* (Fig. 2 *B* and *C*). Notably, knockdown of one candidate gene, *ARHGAP9*, led to a significant (+49%) increase in the delivery of $\mathbf{2}^{R}$ to the nucleus and cytosol (Fig. 2 *B* and *C*); this finding suggests that inhibitors of ARHGAP9 could improve endosomal release. It is also notable that genes whose knockdown strongly reduced the delivery of $\mathbf{2}^{R}$ encompass multiple cellular activities related to membrane homeostasis, including membrane tethering (*VPS39*, *RAB2A*), glycosylphosphatidylinositol-anchor biosynthesis (*PIGW*), thioesterases (*LYPLA1*), and cytoskeletal genes (*PXN*, *ZYX*). The remaining eight genes consisted of *DOCK4* and seven olfactory receptors (ORs: *OR4C6*, *OR4F15*, *OR51E1*, *OR51Q1*, *OR52N1*, *OR5M8*, *OR8D1*), which were eventually classified as false-positives. In summary, of the 28 genes identified in the GIGT high-throughput screen, knockdown of 6 strongly inhibited cytosolic access, knockdown of 13 moderately

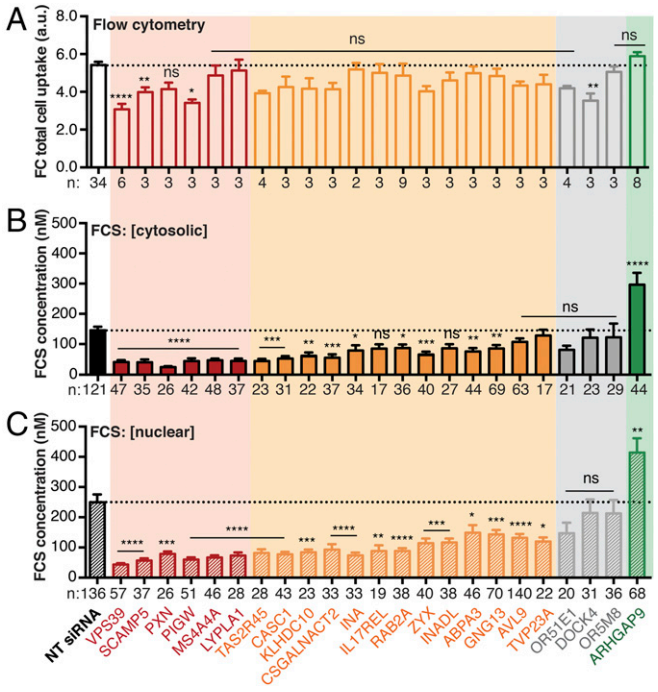

Fig. 2. Categorizing candidate genes using FC and FCS. Knockdowns were achieved by transfecting Saos-2 cells with siGENOME SMARTpool siRNA and Lipofectamine RNAiMAX for 72 h according to the manufacturer's protocol. Cells were treated with CPMP $\mathbf{2}^{R}$ (600 nM) for 30 min and exogenously bound CPMP was removed with TrypLE Express. Cells were then evaluated using FC to assess the levels of whole-cell fluorescence intensity and using FCS to calculate the concentration of $\mathbf{2}^{R}$ in the cytosol and nucleus. FC and FCS data illustrating the effects of gene knockdowns on total cellular fluorescence (*A*), the cytosolic (*B*), and nuclear (*C*) localization of $\mathbf{2}^{R}$ relative to the effects of nontargeting (RISC-free) siRNA (NT siRNA). Knockdown of genes shown in red strongly inhibit (>70%) intracellular (cytosolic and nuclear) access of $\mathbf{2}^{R}$. Knockdown of genes shown in orange moderately inhibit (30–70%) intracellular access of $\mathbf{2}^{R}$. Knockdown of the *ARHGAP9* gene shown in green promotes (149%) cytosolic access of $\mathbf{2}^{R}$. (*A*) FC: total cell uptake, fluorescence intensity at 585 nm. Each data point (*n*) represents one biological replicate. For each FC replicate, the median fluorescence intensity at 585 nm was measured for at least 10,000 Saos-2 cells (gated for live cells). (*B* and *C*) FCS: cytosolic and nuclear concentration (nM). Each data point (*n*) denotes a 50-s FCS measurement recorded in a single cell. Error bars represent the SEM. $^{****}P < 0.0001$, $^{***}P < 0.001$, $^{**}P < 0.01$, $^{*}P < 0.05$, and not significant (ns) for $P > 0.05$ from one-way ANOVA with Dunnett post hoc test.

inhibited cytosolic access, and knockdown of 1 gene promoted cytosolic access (*SI Appendix*, Fig. S6*C*). These data provide evidence that we successfully screened and prioritized genes that primarily regulate intracellular trafficking—with 20 of 28 genes affected by FCS—and not overall uptake, with only 4 genes affected by FC.

Hydrocarbon-stapled α-helical peptides are a promising class of therapeutic candidates because they can exhibit improved pharmacological properties—such as increased binding affinity, proteolytic resistance, and cell permeability—compared with staple-free analogs (52–54). Although hydrocarbon-stapled peptides lack the defined array of arginine side chains that characterizes CPMPs **1** and **2**, they reach the cytosol with high efficiency. In particular, the hydrocarbon-stapled peptide SAH-p53-8^{R} ($\mathbf{3}^{R}$) achieves average intracellular concentrations (as determined by FCS in HeLa or Saos-2 cells) that are only 10–50% lower than those attained by ZF5.3^{R} ($\mathbf{2}^{R}$), depending on the cell line used (12). To investigate whether **2** and **3** share a common mode of endosomal release, Saos-2 cells were treated with pooled siRNAs targeting the set of 20 candidate genes, treated with $\mathbf{3}^{R}$ (600 nM), and both whole-cell uptake and cytosolic delivery were quantified with FC and FCS, as described above (*SI Appendix*, Fig. S6*D*).

A plot showing the percent effect of each statistically significant knockdown (that is, significant for both $\mathbf{2}^{R}$ and $\mathbf{3}^{R}$ by one-way ANOVA with Dunnett post hoc test) on the cytosolic localization of $\mathbf{2}^{R}$ or $\mathbf{3}^{R}$ showed moderate correlation (Pearson's $r = 0.47$, $P = 0.17$) (*SI Appendix*, Fig. S7*A*). Knockdown of five genes—*VPS39*, *INA*, *LYPLA1*, *KLHDC10*, and *CASC1*—strongly (>50%) inhibited the appearance of both $\mathbf{2}^{R}$ and $\mathbf{3}^{R}$ in the cytosol (*SI Appendix*, Fig. S7*A*, blue open circles). Knockdown of another four genes—*MS4A4A*, *TAS2R45*, *RAB2A*, and *APBA3*—resulted in a moderate (30–50%) decrease in the appearance of both $\mathbf{2}^{R}$ and $\mathbf{3}^{R}$ in the cytosol (*SI Appendix*, Fig. S7*A*, green dots). Knockdown of AVL9, although statistically significant, did not have a strong percent-effect on the ability of either $\mathbf{2}^{R}$ or $\mathbf{3}^{R}$ to reach the cytosol (*SI Appendix*, Fig. S7*A*). When the effects of these gene knockdowns on overall uptake of $\mathbf{2}^{R}$ and $\mathbf{3}^{R}$ are plotted, the effects are small, as expected (*SI Appendix*, Fig. S7*B*). Overall, the observed correlation between the effects of gene knockdowns on the cytosolic localization of CPMP $\mathbf{2}^{R}$ and hydrocarbon-stapled peptide $\mathbf{3}^{R}$ suggests that these genes play common roles in the intracellular trafficking of these two molecular families. The five genes that most strongly regulate cytosolic delivery of both $\mathbf{2}^{R}$ or $\mathbf{3}^{R}$ can be divided into four categories: (*i*) genes with known roles in endocytic trafficking (*VPS39*), (*ii*) genes involved in the processing of post hoc translational protein modifications (*LYPLA1*), (*iii*) genes involved in RNA processing (*CASC1*), and (*iv*) genes with poorly characterized or unknown functions (*INA* and *KLHDC10*).

siRNA Depletion of HOPS but Not CORVET Inhibits the Cytosolic Delivery of CPMPs and CPPs $\mathbf{1}^{R}$–$\mathbf{5}^{R}$. The goal of the RNAi screen was to identify candidate genes that significantly enhance or inhibit the intracellular localization of multiple CPMPs and CPPs. One gene transcript, when depleted, strongly inhibited the cellular uptake and cytosolic delivery of both CPMP $\mathbf{2}^{R}$ and stapled peptide $\mathbf{3}^{R}$: the *VPS39* gene, also known as hVamp6. *VPS39* encodes an 875-residue protein that is conserved in eukaryotes (55) and is one of six protein subunits comprising the HOPS membrane-tethering complex (*SI Appendix*, Fig. S7*C*). Working with VPS41 and various effector proteins (56, 57), VPS39 recruits the HOPS complex to endosomes positive for the small GTPase Rab7, such as maturing endosomes (MEs) (Rab5^{+}/Rab7^{+}) and LEs (Rab7^{+}). The remaining four core HOPS subunits—VPS11, VPS16, VPS18, and VPS33A—are believed to primarily serve a structural role (57). A fully assembled HOPS complex is required to initiate fusion of Rab7^{+} maturing and LEs into LYs. Depletion of any subunit delays LY maturation and inhibits cargo degradation (57–59). HOPS is closely related to a structurally similar complex called CORVET (*SI Appendix*, Fig. S7*C*), which precedes HOPS along the endocytic pathway by promoting the fusion of Rab5^{+} early endosomes (EEs) and MEs (60). CORVET shares four core subunits with HOPS but contains TGFBRAP1 and VPS8 (60) in place of VPS39 and VPS41.

Having identified VPS39 as a key regulator of the cytosolic delivery of $\mathbf{2}^{R}$ and $\mathbf{3}^{R}$, we next asked whether the observed effect was dependent on VPS39 alone or also on the other unique protein subunit of the HOPS complex: VPS41. Saos-2 cells transfected with a nontargeting (RISC-free) or a pool of four VPS41-targeting siRNAs were treated with $\mathbf{1}^{R}$–$\mathbf{3}^{R}$ (600 nM) for 30 min and analyzed using both FC and FCS, as described above (Fig. 3*A*). In our primary screen, we found that siRNAs against VPS41 displayed a mild inhibitory effect on GR*-eGFP translocation in the presence of $\mathbf{1}^{Dex}$ (27% mean percent effect, 1.58 *Z*-score, 1.65 SSMD), which was below our hit threshold. Here, upon VPS41 depletion, we observed a moderate decrease (−14%) in overall uptake and a strong (−78%) decrease in the average intracellular concentration of $\mathbf{1}^{R}$ (Fig. 3*B*). Similarly, we

also observed a moderate decrease (−27%) in overall uptake and a strong (−71%) decrease in the average intracellular concentration for $\mathbf{2}^{R}$ (Fig. 3*C*); these changes are comparable to those observed after VPS39 knockdown. In VPS41-depleted cells treated with hydrocarbon-stapled peptide $\mathbf{3}^{R}$, we also observed a significant decrease in overall uptake (−27%) and in the average intracellular delivery (−55%) by FCS (Fig. 3*D*); these changes are also similar to those observed after VPS39 knockdown. In contrast, no significant decreases in overall uptake or cytosolic localization of $\mathbf{1}^{R}$, $\mathbf{2}^{R}$, or $\mathbf{3}^{R}$ were observed upon depletion of the CORVET-specific subunits TGFBRAP1 and VPS8; in fact, depletion of the TGFBRAP subunit led to significant increases in both overall uptake and cytosolic concentration of $\mathbf{2}^{R}$ and $\mathbf{3}^{R}$ (Fig. 3 *C* and *D*). Taken together, these data support a hypothesis in which both unique components of the HOPS complex, VPS39 and VPS41, are required to allow cytosolic access of CPMPs $\mathbf{1}^{R}$ and $\mathbf{2}^{R}$ and the hydrocarbon-stapled peptide $\mathbf{3}^{R}$.

Because of unusual diffusion dynamics observed for CPPs $\mathbf{4}^{R}$ and $\mathbf{5}^{R}$ in cultured cells (*SI Appendix*, Table S2), we were unable to perform FCS experiments to evaluate whether their delivery to the cytosol required HOPS subunits or activity. We were able to estimate their relative delivery into the cytosol on the basis of fluorescence intensity values obtained during FCS measurements (without autocorrelation); these values are proportional to the intracellular concentration in the confocal volume (*SI Appendix*, Fig. S8). Knockdown of either VPS39 or VPS41 led to a significant (23–35%) decrease in whole-cell uptake of $\mathbf{4}^{R}$ or $\mathbf{5}^{R}$ (as determined by FC) and a 46–62% decrease in their average intracellular fluorescence intensity (as determined by FCS without autocorrelation) (Fig. 3 *E* and *F*). In contrast, knockdown of the CORVET subunits TGFBRAP1 or VPS8 led to either no change ($\mathbf{5}^{R}$) or a 30% increase ($\mathbf{4}^{R}$) in overall uptake (as determined by FC). Knockdown of TGFBRAP1 led to no change in the average intracellular fluorescence intensity of $\mathbf{4}^{R}$ or $\mathbf{5}^{R}$ (as determined by FCS without autocorrelation), while knockdown of VPS8 either stimulated ($\mathbf{4}^{R}$) or had no effect ($\mathbf{5}^{R}$) on the average cytosolic fluorescence intensity as determined by FCS without autocorrelation.

Taken together, these data show that HOPS-specific subunits VPS39 and VPS41, but not CORVET-specific subunits TGFBRAP1 and VPS8, are required for the cytosolic delivery of all CPMP/CPPs tested herein. These CPMPs and CPPs differ significantly in their intrinsic ability to reach the cytosol (*SI Appendix*, Fig. S4*A*), but in all cases this ability demands an active HOPS complex. Importantly, the more active CPMPs **1** and **2** are significantly more sensitive to knockdown of the HOPS subunit VPS39 than hydrocarbon-stapled peptide **3** or CPPs **4** and **5**; knockdown of VPS39 led to 79% and 74% decrease in the cytosolic concentrations of CPMPs **1** and **2**, whereas the decreases observed for hydrocarbon-stapled peptide **3** and CPPs **4** and **5** ranged from 49 to 56%. These data suggest that even though all peptides require HOPS-dependent fusion of $Rab7^{+}$ endosomes to access the cytosol, CPMPs **1** and **2** may be more strongly dependent on this pathway—or make more efficient use of it—than hydrocarbon-stapled peptide **3** and CPPs **4**–**5**.

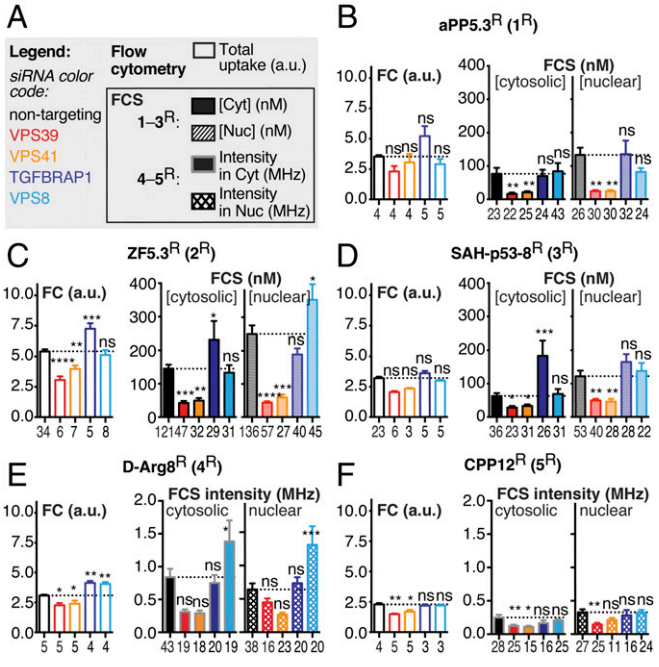

Fig. 3. Efficient cytosolic trafficking of all CPMPs and CPPs requires the human HOPS complex. (*A*) Figure legend. (*B*–*F*) The effect of VPS39 and VPS41 knockdown (HOPS-specific subunits) compared with TGFBRAP1 and VPS8 knockdown (CORVET-specific subunits) on both overall uptake (FC) and cytosolic access (FCS) of $\mathbf{1}^{R}$ (*B*), $\mathbf{2}^{R}$ (*C*), $\mathbf{3}^{R}$ (*D*), $\mathbf{4}^{R}$ (*E*), and $\mathbf{5}^{R}$ (*F*) relative to the effect of nontargeting siRNA (NT siRNA). FC: total cell uptake, fluorescence intensity at 585 nm in arbitrary units (a.u.). *n* refers to the number of biological replicates. For each FC replicate, the median fluorescence intensity at 585 nm was measured for at least 10,000 Saos-2 cells (gated for live cells). FCS: cytosolic and nuclear concentration (nM) (*B*–*D*) or intensity (MHz) (*E* and *F*). Each data point (*n*) denotes one 50-s FCS measurement recorded in the nucleus or cytosol of a single Saos-2 cell with (*B*–*D*) or without (*E* and *F*) autocorrelation. Error bars represent the SEM. $^{****}P < 0.0001$, $^{***}P < 0.001$, $^{**}P < 0.01$, $^{*}P < 0.05$, not significant (ns) for $P > 0.05$ from one-way ANOVA with Dunnett post hoc test.

HOPS Remains Active upon Treatment with CPMPs and CPPs 1–5. Although the experiments described above indicate that efficient cytosolic delivery of CPMP/CPPs **1**–**5** demands the presence of a fully assembled HOPS complex, they do not discriminate between two limiting explanations for this dependence: one in which cytosolic access demands the activity of the HOPS complex and another in which cytosolic access demands the inhibition of this activity. To discriminate between these two possibilities, we monitored HOPS activity in the presence of CPMPs $\mathbf{1}^{UL}$–$\mathbf{5}^{UL}$ using a previously reported fluorescence colocalization protocol that quantifies HOPS-dependent delivery of dextran to lysosomal compartments (58, 59, 61). In this assay, the endocytic system is flooded with Alexa Fluor 488-tagged dextran for 2 h, after which the cells are washed and replated in dextran-free media, incubated for 1 h, stained with Magic Red, and imaged immediately by confocal microscopy (*SI Appendix*, Fig. S9*A*). Magic Red is a dye that becomes fluorescent in the presence of active cathepsin B, an enzyme exclusively localized to mature LYs. Dextran is only delivered to LY compartments if endosomal fusion of $Rab7^{+}$ endosomes occurs. This process requires a fully assembled and functional HOPS complex (58, 59).

To validate this assay, we first measured the effect of HOPS-specific subunit depletion on the colocalization of Magic Red with dextran. Saos-2 cells were transfected with siRNA pools targeting either VPS39 or VPS41, or with a nontargeting siRNA as a negative control. After 72 h, cells were treated as described above and the colocalization of dextran and Magic Red was calculated using ImageJ (33). In untreated and nontargeting siRNA-treated Saos-2 cells, the colocalization of Alexa Fluor 488-dextran and Magic Red was characterized by Manders coefficients of 0.30 ± 0.030 and 0.23 ± 0.020, respectively; these values represent the fraction of dextran-containing vesicles that also contain cathepsin B and are comparable to those measured previously (61, 62) (*SI Appendix*, Fig. S9 *B* and *C*). As expected, depletion of HOPS-specific subunits VPS39 and VPS41 significantly reduced the colocalization of Alexa Fluor 488-dextran and Magic Red, leading to significantly lower Manders coefficients of 0.11 ± 0.024 and 0.12 ± 0.016, respectively (*SI Appendix*, Fig. S9 *B* and *C*).

With a validated assay in hand, we next asked whether addition of CPMPs or CPPs $\mathbf{1}^{UL}$–$\mathbf{5}^{UL}$ had an observable effect on the

intrinsic activity of the HOPS complex. Saos-2 cells were pretreated with unlabeled CPMPs $\mathbf{1}^{UL}$–$\mathbf{5}^{UL}$ at 600 nM for 30 min and labeled with Alexa Fluor 488-dextran and Magic Red, as described above (*SI Appendix*, Fig. S9*D*). In cells treated with CPMPs/CPPs $\mathbf{1}^{UL}$–$\mathbf{5}^{UL}$, the colocalization of Alexa Fluor 488-dextran and Magic Red was characterized by Manders coefficients that ranged from 0.27 ± 0.030 (when treated with $\mathbf{5}^{UL}$) to 0.33 ± 0.030 (when treated with $\mathbf{1}^{UL}$), well within the range of values measured in cells that had not been treated with CPMPs or CPPs (*SI Appendix*, Fig. S9 *E* and *F*). We conclude that the treatment of Saos-2 cells with CPMPs **1**–**5** neither inhibits nor enhances HOPS-mediated endosomal fusion. As a whole, our studies suggest that the endosomal escape of all CPMPs and CPPs tested is dependent on the presence of a functional, active HOPS complex.

How Does HOPS Mediate Endosomal Escape? HOPS is required for the fusion of Rab7$^+$ endosomes, a process initiated by HOPS-mediated membrane tethering and completed by the mechanical action of SNARE proteins and the HOPS complex itself (63). To gain an improved understanding of the mechanism with which HOPS mediates endosomal escape, we used confocal microscopy to determine the location of $\mathbf{2}^R$ within the endosomal system. Confocal microscopy studies were performed with Saos-2 cells expressing either Rab5-GFP, a marker of EEs and MEs, Rab7-GFP, a marker of MEs and LEs, or Lamp1-GFP, a marker for LEs and LYs (64). After expressing these GFP markers in Saos-2 cells for 16 h, we treated cells with $\mathbf{2}^R$ (300 nM) for 30 min. Total uptake of $\mathbf{2}^R$ (as determined using FC) was similar whether cells expressed a GFP-tagged protein or not (*SI Appendix*, Fig. S10*A*). Analysis of the extent of colocalization of $\mathbf{2}^R$ with each GFP marker revealed low colocalization between $\mathbf{2}^R$ and Rab5-GFP (Pearson's $r = 0.20 \pm 0.019$) but high colocalization with Rab7-GFP ($r = 0.55 \pm 0.034$) and Lamp1-GFP ($r = 0.58 \pm 0.027$) (Fig. 4 *A* and *C*). These data are consistent with earlier studies showing that $\mathbf{2}^R$ colocalizes moderately with Rab5$^+$ endosomes and strongly with Rab7$^+$ endosomes (11). As observed previously, Lamp1-GFP overexpression led to endosome clustering (65). To better resolve the location of $\mathbf{2}^R$, we treated Saos-2 cells with the small molecule YM201636, an inhibitor of the phosphoinositide kinase PIK-fyve that enlarges Rab7$^+$ endolysosomes (66, 67). YM201636 preincubation had only a modest effect on the extent of colocalization of $\mathbf{2}^R$ with each GFP marker (Rab5-GFP, $r = 0.034 \pm 0.025$; Rab7-GFP, $r = 0.57 \pm 0.043$; Lamp1-GFP, $r = 0.73 \pm 0.023$) (Fig. 4 *B* and *C*). Line profiles across these enlarged vesicles (plots of fluorescence intensity as a function of position) show clearly separable distributions of fluorescence due to GFP (green) and lissamine rhodamine B (red) (Fig. 4 *D* and *E*). These distributions suggest that $\mathbf{2}^R$ resides primarily within Rab7$^+$ and Lamp1$^+$ vesicles and not on their surface.

HOPS Is Required to Deliver CPMP 2 to Lamp1$^+$ Endosomes. The tethering activity of the HOPS complex is an essential element of the membrane fusion cycle, bringing Rab7$^+$ endosomal membranes in proximity to facilitate fusion into Lamp1$^+$ LEs and LYs (68). Genetic depletion of HOPS subunits VPS39 or VPS41 reduces HOPS-mediated fusion of Rab7$^+$ endosomes and impairs the formation of Lamp1$^+$ LEs and LYs (58). As genetic depletion of the same HOPS subunits decreases trafficking of CPMP **2** into the cytosol and nucleus (Fig. 3*C*), we hypothesized that HOPS is required to guide CPMP **2** to Lamp1$^+$ endosomes. To test this hypothesis, we transfected Saos-2 cells with a nontargeting siRNA as well as with siRNAs against the HOPS subunit VPS39 and, as a second control, the CORVET subunit TGFBRAP1. Control cells transfected with a nontargeting (RISC-free) siRNA and treated with $\mathbf{2}^{SiR}$ [in which **2** is tagged with a silicon-rhodamine (SiR) dye that emits at 660–670 nm (69)] showed virtually no colocalization between $\mathbf{2}^{SiR}$ and Rab5-GFP ($r = 0.05 \pm$

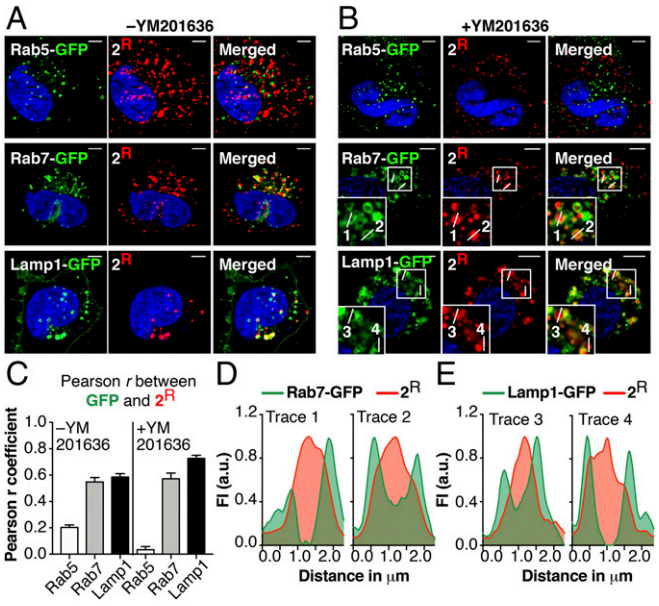

Fig. 4. CPMP **2** localizes to the lumen of LEs and LYs. Saos-2 cells were transduced with Rab5-, Rab7-, or Lamp1-GFP for 18 h using CellLight Reagents (BacMam 2.0). Cells were washed, incubated with CPMP $\mathbf{2}^R$ (300 nM), stained with Hoechst 33342, lifted with TrypLE, and replated into microscopy slides. Cells were then incubated in media ±YM201636 for 1 h. (*A* and *B*) Representative live-cell confocal fluorescence microscopy images of Saos-2 cells in media without (*A*) or with (*B*) YM201636. (Scale bars: 5 μm.) (*C*) Pearson correlation coefficients characterizing colocalization of GFP markers and $\mathbf{2}^R$ in the presence and absence of YM201636. (*D* and *E*) Fluorescence intensity line profiles of endosomes 1–4 (displayed in *B*) showing the relative location of emission due to $\mathbf{2}^R$ (red) and either (*D*) Rab7-GFP or (*E*) Lamp1-GFP (green).

0.01), moderate colocalization with Rab7-GFP ($r = 0.25 \pm 0.016$), and good colocalization with Lamp1-GFP ($r = 0.57 \pm 0.027$) (Fig. 5 *A* and *D*). These colocalization values are virtually identical to those observed using $\mathbf{2}^R$ (Fig. 4*C*), indicating that the localization of **2** is independent of dye identity. Again, total uptake of $\mathbf{2}^{SiR}$ (as determined using FC) was similar whether cells expressed a GFP-tagged protein or not (*SI Appendix*, Fig. S10*B*). Cells depleted of the HOPS subunit VPS39 also showed virtually no colocalization of $\mathbf{2}^{SiR}$ with Rab5-GFP ($r = 0.05 \pm 0.01$) and moderate colocalization with Rab7-GFP ($r = 0.21 \pm 0.016$). But in this case, the colocalization of $\mathbf{2}^{SiR}$ with Lamp1-GFP ($r = 0.35 \pm 0.026$) was significantly lower compared with control cells (Fig. 5 *B* and *D*). We also observed the previously reported fragmentation phenotype associated with HOPS knockdown (58): an increased number of endosomes accompanied by an overall decrease in endosome size. No such changes were observed in CORVET-deficient cells; in this case we observed virtually no colocalization of $\mathbf{2}^{SiR}$ with Rab5-GFP ($r = 0.083 \pm 0.013$), moderate colocalization with Rab7-GFP ($r = 0.21 \pm 0.015$), and high colocalization with Lamp1-GFP ($r = 0.47 \pm 0.021$) (Fig. 5*C*). Notably, although the clustering due to Lamp1-GFP overexpression (65) was observed in cells treated with a nontargeting siRNA or with siRNAs against the CORVET subunit TGFBRAP1 (Fig. 5 *A* and *C*), it was not observed in cells treated with an siRNA against the HOPS subunit VPS39 (Fig. 5*B*). These data indicate that knockdown of HOPS but not CORVET inhibits trafficking of $\mathbf{2}^{SiR}$ to Lamp1$^+$ LEs and LYs and validates the hypothesis that HOPS activity is required to guide CPMP **2** to Lamp1$^+$ endosomes before escape into the cytosol.

Closer examination of enlarged endosomes in Rab7- or Lamp1-GFP–expressing cells revealed the presence of smaller vesicles within the boundaries of LE membranes, as shown in *SI Appendix*, Fig. S11 *A* and *B* and in two movies of cells expressing

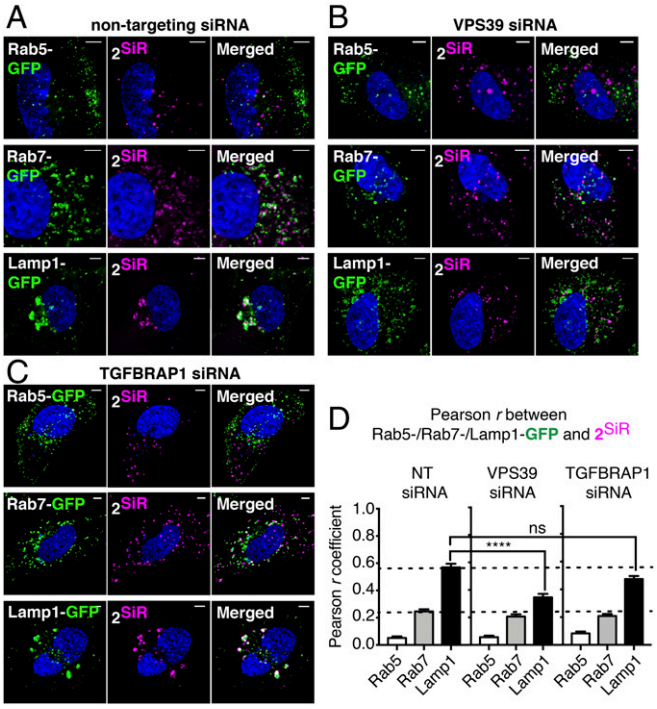

Fig. 5. HOPS knockdown inhibits trafficking of CPMP **2** to Lamp1$^+$ LEs and LYs. Saos-2 cells were transfected with pooled siRNAs against VPS39 or a nontargeting (NT) control siRNA (RISC-free) for 72 h. Rab5-, Rab7-, or Lamp1-GFP were expressed by transduction with CellLight Reagents (BacMam 2.0) for 18 h. Cells were incubated with CPMP $\mathbf{2}^{SiR}$ (600 nM) for 30 min and nuclei were stained with Hoechst 33342 (300 nM) for 5 min. Cells were lifted using TrypLE Express to remove exogenously bound CPMP and replated for confocal microscopy. (*A*–*C*) Representative live-cell confocal microscopy images of Saos-2 cells transfected with an NT (RISC-free) siRNA (*A*), VPS39-targeting siRNAs (*B*), or TGFBRAP1-targeting siRNAs (*C*). (Scale bars: 5 μm.) (*D*) Pearson correlation coefficients between GFP markers and $\mathbf{2}^{SiR}$ in nontargeting siRNA control cells, VPS39, and TGFBRAP1 knockdown cells.

Lamp1-GFP and treated with $\mathbf{2}^{R}$ (white arrows in *SI Appendix*, Fig. S11 *A* and *B* and Movies S1 and S2). LEs are characterized, among other properties, by the presence of ILVs (64). To determine whether the smaller $\mathbf{2}^{R}$-containing vesicles observed in LEs represent ILVs, we used a known ILV marker, the lipid *N*-Rh-PE, a lissamine rhodamine B-tagged version of 1,2-dipalmitoyl-*sn*-glycero-3-phosphoethanolamine (70) (*SI Appendix*, Fig. S11*C*). *N*-Rh-PE is internalized via the endocytic pathway into ILVs (71–73) before it is eventually secreted in exosomes (70, 72, 74). As expected (70), *N*-Rh-PE localizes to Rab7-GFP$^+$ MEs and LEs ($r = 0.39 \pm 0.050$) and Lamp1-GFP$^+$ LEs and LYs ($r = 0.45 \pm 0.031$), but not to Rab5-GFP$^+$ EEs and MEs endosomes ($r = 0.104 \pm 0.004$) (*SI Appendix*, Fig. S11 *D* and *F*). Saos-2 cells treated with $\mathbf{2}^{SiR}$ alone showed a colocalization profile that mirrored that of $\mathbf{2}^{R}$, as expected (compare Fig. 4 *A* and *C* to *SI Appendix*, Fig. S11 *E* and *G*). Saos-2 cells treated with both *N*-Rh-PE and $\mathbf{2}^{SiR}$ showed significant colocalization ($r = 0.53 \pm 0.028$) (*SI Appendix*, Fig. S11 *H* and *I*), providing evidence that CPMP $\mathbf{2}^{SiR}$ indeed localizes to ILVs and to Rab7$^+$ and Lamp1$^+$ vesicles that contain ILVs.

We also performed a four-color confocal microscopy experiment to visualize Saos-2 cells expressing Rab5-, Rab7-, or Lamp1-GFP and treated with *N*-Rh-PE, $\mathbf{2}^{SiR}$, as well as Hoechst 33342 (*SI Appendix*, Fig. S12). As expected, we observed virtually no colocalization of $\mathbf{2}^{SiR}$ with Rab5-GFP ($r = 0.071 \pm 0.014$) but good colocalization with Rab7- ($r = 0.35 \pm 0.036$) and Lamp1-GFP ($r = 0.41 \pm 0.037$). Also as expected, we observed minimal colocalization of *N*-Rh-PE with Rab5-GFP ($r = 0.078 \pm 0.023$) and good colocalization with Rab7- ($r = 0.39 \pm 0.039$) and Lamp1-GFP ($r = 0.43 \pm 0.045$) (*SI Appendix*, Fig. S12 *A* and *C*). Importantly, good colocalization between $\mathbf{2}^{SiR}$ and *N*-Rh-PE was observed in Saos-2 cells regardless of which endosomal marker was present (*SI Appendix*, Fig. S12 *A* and *C*). To enlarge Rab7$^+$ endolysosomes for better resolution, we again treated Saos-2 cells with YM201636 (66, 67) (*SI Appendix*, Fig. S12*B*). Pearson's *r* values were similar in cells with and without YM201636 present (*SI Appendix*, Fig. S12*D*). By generating line profiles of endosomes displayed in *SI Appendix*, Fig. S12*B*, we again observed minimal overlap between the signal due to Rab7-GFP or Lamp1-GFP and either CPMP $\mathbf{2}^{SiR}$ or the ILV marker *N*-Rh-PE (*SI Appendix*, Fig. S12 *E* and *F*). These results further support the conclusion that CPMP **2** colocalizes with ILVs found within Rab7$^+$ and Lamp1$^+$ LEs.

Discussion

Unlike many small molecules, most proteins and peptides with therapeutic potential must circumnavigate a complex journey to access the cytosol or nucleus of mammalian cells. There is compelling evidence that this journey often involves endocytosis (75, 76), the natural cellular process by which extracellular material is taken up into vesicles formed from the plasma membrane. However, the pathway into the cytosol requires not just uptake into endocytic vesicles, but also endosomal release, and this second step is widely recognized as the bottleneck hindering the efficient delivery of peptidic materials into the cytosol and nucleus (11, 77–85). We discovered several years ago that CPMPs, such as ZF5.3 (11, 86, 87), overcome this bottleneck to reach the cytosol with exceptional efficiency, both with (16) and without (12) an appended protein cargo. Here, we sought to understand the cellular processes that support the trafficking of CPMPs into the cytosol. First, using two complementary cell-based assays, we ruled out the most obvious mechanism of endosomal release: a partial or complete disruption of endosomal integrity. Next, using a spectrum of tools, including a genome-wide RNAi screen, quantitative FCS, and live-cell, multicolor confocal imaging, we identified *VPS39*—a gene encoding a subunit of the HOPS complex—as a critical determinant in the trafficking of CPMPs to the cytosol. CPMPs neither inhibit nor activate HOPS activity; indeed, HOPS activity is essential to ensure cytosolic access of CPMPs as well as other CPPs and hydrocarbon-stapled peptides. Subsequent multicolor confocal imaging studies identified CPMPs within the endosomal lumen of Rab7$^+$ and Lamp1$^+$ endosomes that are the products of HOPS-mediated fusion and show that within these vesicles, CPMPs colocalize with ILVs. Finally, we showed that depletion of HOPS activity decreases the amount of CPMP that reaches Lamp1$^+$ vesicles. Although previous work reported that ZF5.3^{R} colocalizes with Rab5-GFP and implied release from Rab5$^+$ endosomes, the extent of colocalization with Rab7-GFP and Lamp1-GFP was not previously examined (11); the more extensive studies here suggest that release from ILV-containing Lamp1$^+$ vesicles contributes more to cytosolic localization. In addition, previous studies were performed in Rab5^{Q79L}-expressing cells; while it has been shown that Rab5^{Q79L+} endosomes do not shed Rab5, such vesicles still recruit a substantial amount of Rab7 and are Lamp1$^+$ (88). Because Rab5^{Q79L+} endosomes recruit later vesicle markers, the lack of inhibition of the cytosolic delivery of aPP5.3 and ZF5.3 upon Rab5^{Q79L} expression may not necessarily suggest that Rab5 alone is sufficient for endosomal escape. Overall, our results imply that the HOPS-dependent tethering and membrane fusion process is required because it guides CPMPs into Rab7$^+$ and Lamp1$^+$ endosomes that contain ILVs and that this environment is prerequisite for efficient endosomal escape.

The HOPS complex has also been implicated in the cytosolic trafficking of numerous bacterial, fungal, and viral pathogens,

including coronavirus (CoV) (89, 90), the Ebola virus (91), *Fusarium graminearum* (92), *Candida albicans* (93), *Cryptococcus neoformans* (94), and *Aspergillus nidulans* (95). In particular, although their genomes lack sequences encoding a canonical penta-Arg motif, both CoV and Ebola require HOPS during the later steps of their postulated mechanism of cell entry: after the viral particle has been endocytosed but before it reaches the cytosol. Passage of CoV into the cytosol requires processing of viral proteins by lysosomal proteases to enable fusion with lysosomal membranes and release into the cytosol; HOPS depletion prevents CoV from reaching the LY and thus fusion and release cannot occur (90). Although CPMPs such as **2** also require HOPS to reach LEs and LYs, there is no evidence that processing by lysosomal proteases is involved: greater than >90% of $\mathbf{2}^{R}$ is intact when delivered to the HeLa cell cytosol (12), and the in vivo diffusion coefficients reported for $\mathbf{2}^{R}$ in the HeLa cell cytosol (12) are virtually identical to those reported here (*SI Appendix*, Table S2).

We propose three limiting models for escape of a CPMP from Lamp1^{+} endosomes that are consistent with the experimental findings reported herein. The first invokes a direct interaction between a CPMP/CPP located near the surface of a Rab7^{+} LE and a component of the HOPS complex, perhaps VPS39 or VPS41, which effectively shuttles the CPMP or CPP from an endosome into the cytosol (direct shuttle model). The second model also positions the CPMP/CPP near the surface of a Rab7^{+} LE but lacks a direct HOPS–CPMP/CPP interaction; in this case HOPS facilitates escape of the CPMP/CPP during the fusion process (96, 97) (fusion-mediated escape model). In the third model, the CPMP or CPP escapes after HOPS-dependent fusion is complete, when MEs and LEs have fused into compartments containing ILVs that may undergo back-fusion to move the CPMP into the cytosol (ILV-mediated escape model). Indeed, some evidence for CPP–ILV interactions have been reported (38). Although further work is needed to elucidate the very final steps taken as a CPP or CPMP circumnavigates into the cytosol, we anticipate that the identification of HOPS as a critical determinant of endosomal release will aid the development of next-generation biologics that overcome the limitations imposed by cellular membranes.

Materials and Methods

For more information on reagents, chemicals, and experimental model systems, please consult the *SI Appendix*. The *SI Appendix* also includes detailed procedures for the synthesis of all CPMPs and CPPs studied herein, methods and assays related to FCS and all cell-based assays, including the siRNA screen and confocal microscopy-based assays.

ACKNOWLEDGMENTS. We thank Prof. Elizabeth Rhoades and Dr. Xiaohan Li for initial help with fluorescence correlation spectroscopy, the Yale Center for Molecular Discovery for assistance with the RNAi screen, and Dr. Andreas Ernst for comments on the manuscript. This work was supported by National Institutes of Health Grants R01 GM74756 and CA170741 (to A. Schepartz). A. Steinauer was supported by an International Student Research Fellowship from the Howard Hughes Medical Institute. S.L.K. acknowledges National Science Foundation Graduate Research Fellowship Program Grant DGE1752134.

1. Lagassé HA, et al. (2017) Recent advances in (therapeutic protein) drug development. *F1000 Res* 6:113.
2. Schatz G, Dobberstein B (1996) Common principles of protein translocation across membranes. *Science* 271:1519–1526.
3. Green M, Loewenstein PM (1988) Autonomous functional domains of chemically synthesized human immunodeficiency virus tat trans-activator protein. *Cell* 55: 1179–1188.
4. Frankel AD, Pabo CO (1988) Cellular uptake of the tat protein from human immunodeficiency virus. *Cell* 55:1189–1193.
5. Derossi D, Joliot AH, Chassaing G, Prochiantz A (1994) The third helix of the Antennapedia homeodomain translocates through biological membranes. *J Biol Chem* 269: 10444–10450.
6. Guidotti G, Brambilla L, Rossi D (2017) Cell-penetrating peptides: From basic research to clinics. *Trends Pharmacol Sci* 38:406–424.
7. Milletti F (2012) Cell-penetrating peptides: Classes, origin, and current landscape. *Drug Discov Today* 17:850–860.
8. El-Sayed A, Futaki S, Harashima H (2009) Delivery of macromolecules using arginine-rich cell-penetrating peptides: Ways to overcome endosomal entrapment. *AAPS J* 11: 13–22.
9. Zondlo NJ, Schepartz A (1999) Highly specific DNA recognition by a designed miniature protein. *J Am Chem Soc* 121:6938–6939.
10. Chin JW, Schepartz A (2001) Concerted evolution of structure and function in a miniature protein. *J Am Chem Soc* 123:2929–2930.
11. Appelbaum JS, et al. (2012) Arginine topology controls escape of minimally cationic proteins from early endosomes to the cytoplasm. *Chem Biol* 19:819–830.
12. LaRochelle JR, Cobb GB, Steinauer A, Rhoades E, Schepartz A (2015) Fluorescence correlation spectroscopy reveals highly efficient cytosolic delivery of certain penta-arg proteins and stapled peptides. *J Am Chem Soc* 137:2536–2541.
13. Holub JM, Larochelle JR, Appelbaum JS, Schepartz A (2013) Improved assays for determining the cytosolic access of peptides, proteins, and their mimetics. *Biochemistry* 52:9036–9046.
14. Vivès E, Brodin P, Lebleu B (1997) A truncated HIV-1 Tat protein basic domain rapidly translocates through the plasma membrane and accumulates in the cell nucleus. *J Biol Chem* 272:16010–16017.
15. Bernal F, et al. (2010) A stapled p53 helix overcomes HDMX-mediated suppression of p53. *Cancer Cell* 18:411–422.
16. Wissner RF, Steinauer A, Knox SL, Thompson AD, Schepartz A (2018) Fluorescence correlation spectroscopy reveals efficient cytosolic delivery of protein cargo by cell-permeant miniature proteins. *ACS Cent Sci* 4:1379–1393.
17. Maiolo JR, 3rd, Ottinger EA, Ferrer M (2004) Specific redistribution of cell-penetrating peptides from endosomes to the cytoplasm and nucleus upon laser illumination. *J Am Chem Soc* 126:15376–15377.
18. Wender PA, et al. (2000) The design, synthesis, and evaluation of molecules that enable or enhance cellular uptake: Peptoid molecular transporters. *Proc Natl Acad Sci USA* 97:13003–13008.
19. Qian Z, et al. (2016) Discovery and mechanism of highly efficient cyclic cell-penetrating peptides. *Biochemistry* 55:2601–2612.
20. Thurston TL, Wandel MP, von Muhlinen N, Foeglein A, Randow F (2012) Galectin 8 targets damaged vesicles for autophagy to defend cells against bacterial invasion. *Nature* 482:414–418.
21. Maier O, Marvin SA, Wodrich H, Campbell EM, Wiethoff CM (2012) Spatiotemporal dynamics of adenovirus membrane rupture and endosomal escape. *J Virol* 86: 10821–10828.
22. Maejima I, et al. (2013) Autophagy sequesters damaged lysosomes to control lysosomal biogenesis and kidney injury. *EMBO J* 32:2336–2347.
23. Meunier E, et al. (2014) Caspase-11 activation requires lysis of pathogen-containing vacuoles by IFN-induced GTPases. *Nature* 509:366–370.
24. Kilchrist KV, Evans BC, Brophy CM, Duvall CL (2016) Mechanism of enhanced cellular uptake and cytosolic retention of MK2 inhibitory peptide nano-polyplexes. *Cell Mol Bioeng* 9:368–381.
25. Montespan C, et al. (2017) Multi-layered control of Galectin-8 mediated autophagy during adenovirus cell entry through a conserved PPxY motif in the viral capsid. *PLoS Pathog* 13:e1006217.
26. Feeley EM, et al. (2017) Galectin-3 directs antimicrobial guanylate binding proteins to vacuoles furnished with bacterial secretion systems. *Proc Natl Acad Sci USA* 114: E1698–E1706.
27. Paz I, et al. (2010) Galectin-3, a marker for vacuole lysis by invasive pathogens. *Cell Microbiol* 12:530–544.
28. Houzelstein D, et al. (2004) Phylogenetic analysis of the vertebrate galectin family. *Mol Biol Evol* 21:1177–1187.
29. Rabinovich GA, Toscano MA (2009) Turning 'sweet' on immunity: Galectin-glycan interactions in immune tolerance and inflammation. *Nat Rev Immunol* 9:338–352.
30. Aits S, et al. (2015) Sensitive detection of lysosomal membrane permeabilization by lysosomal galectin puncta assay. *Autophagy* 11:1408–1424.
31. Wittrup A, et al. (2015) Visualizing lipid-formulated siRNA release from endosomes and target gene knockdown. *Nat Biotechnol* 33:870–876.
32. Zhao M, et al. (2008) Lipofectamine RNAiMAX: An efficient siRNA transfection reagent in human embryonic stem cells. *Mol Biotechnol* 40:19–26.
33. Schneider CA, Rasband WS, Eliceiri KW (2012) NIH image to ImageJ: 25 years of image analysis. *Nat Methods* 9:671–675.
34. Srinivasan D, et al. (2011) Conjugation to the cell-penetrating peptide TAT potentiates the photodynamic effect of carboxytetramethylrhodamine. *PLoS One* 6:e17732.
35. Erazo-Oliveras A, et al. (2014) Protein delivery into live cells by incubation with an endosomolytic agent. *Nat Methods* 11:861–867.
36. Thiele DL, Lipsky PE (1990) Mechanism of L-leucyl-L-leucine methyl ester-mediated killing of cytotoxic lymphocytes: Dependence on a lysosomal thiol protease, dipeptidyl peptidase I, that is enriched in these cells. *Proc Natl Acad Sci USA* 87:83–87.
37. Uchimoto T, et al. (1999) Mechanism of apoptosis induced by a lysosomotropic agent, L-leucyl-L-leucine methyl ester. *Apoptosis* 4:357–362.
38. Erazo-Oliveras A, et al. (2016) The late endosome and its lipid BMP act as gateways for efficient cytosolic access of the delivery agent dfTAT and its macromolecular cargos. *Cell Chem Biol* 23:598–607.
39. Li M, et al. (2015) Discovery and characterization of a peptide that enhances endosomal escape of delivered proteins in vitro and in vivo. *J Am Chem Soc* 137: 14084–14093.

40. Chakraborti PK, Garabedian MJ, Yamamoto KR, Simons SS, Jr (1991) Creation of "super" glucocorticoid receptors by point mutations in the steroid binding domain. *J Biol Chem* 266:22075–22078.
41. Chakraborti PK, Garabedian MJ, Yamamoto KR, Simons SS (1992) Role of cysteine-640, cysteine-656, and cysteine-661 in steroid binding to rat glucocorticoid receptors. *J Biol Chem* 267:11366–11373.
42. Birmingham A, et al. (2009) Statistical methods for analysis of high-throughput RNA interference screens. *Nat Methods* 6:569–575.
43. Zhang XD, et al. (2007) The use of strictly standardized mean difference for hit selection in primary RNA interference high-throughput screening experiments. *J Biomol Screen* 12:497–509.
44. Parker C, Zhang J-H (2012) High-throughput screening for small-molecule drug discovery. *Development of Therapeutic Agents Handbook*, ed Gad SC (John Wiley & Sons, Hoboken, NJ), pp 147–180.
45. Collinet C, et al. (2010) Systems survey of endocytosis by multiparametric image analysis. *Nature* 464:243–249.
46. Szklarczyk D, et al. (2017) The STRING database in 2017: Quality-controlled protein-protein association networks, made broadly accessible. *Nucleic Acids Res* 45: D362–D368.
47. Laulederkind SJ, et al. (2013) The rat genome database 2013—Data, tools and users. *Brief Bioinform* 14:520–526.
48. Safran M, et al. (2010) GeneCards version 3: The human gene integrator. *Database (Oxford)* 2010:baq020.
49. Jiao X, et al. (2012) DAVID-WS: A stateful web service to facilitate gene/protein list analysis. *Bioinformatics* 28:1805–1806.
50. Huang W, Sherman BT, Lempicki RA (2009) Systematic and integrative analysis of large gene lists using DAVID bioinformatics resources. *Nat Protoc* 4:44–57.
51. Jackson AL, et al. (2003) Expression profiling reveals off-target gene regulation by RNAi. *Nat Biotechnol* 21:635–637.
52. Walensky LD, et al. (2004) Activation of apoptosis in vivo by a hydrocarbon-stapled BH3 helix. *Science* 305:1466–1470.
53. Cromm PM, Spiegel J, Grossmann TN (2015) Hydrocarbon stapled peptides as modulators of biological function. *ACS Chem Biol* 10:1362–1375.
54. Guerlavais V, Sawyer TK (2014) Advancements in stapled peptide drug discovery & development. *Annu Rep Med Chem* 49:331–345.
55. Li Z, Blissard G (2015) The vacuolar protein sorting genes in insects: A comparative genome view. *Insect Biochem Mol Biol* 62:211–225.
56. van der Kant R, et al. (2013) Late endosomal transport and tethering are coupled processes controlled by RILP and the cholesterol sensor ORP1L. *J Cell Sci* 126: 3462–3474.
57. van der Kant R, et al. (2015) Characterization of the mammalian CORVET and HOPS complexes and their modular restructuring for endosome specificity. *J Biol Chem* 290: 30280–30290.
58. Pols MS, ten Brink C, Gosavi P, Oorschot V, Klumperman J (2013) The HOPS proteins hVps41 and hVps39 are required for homotypic and heterotypic late endosome fusion. *Traffic* 14:219–232.
59. Wartosch L, Günesdogan U, Graham SC, Luzio JP (2015) Recruitment of VPS33A to HOPS by VPS16 is required for lysosome fusion with endosomes and autophagosomes. *Traffic* 16:727–742.
60. Perini ED, Schaefer R, Stöter M, Kalaidzidis Y, Zerial M (2014) Mammalian CORVET is required for fusion and conversion of distinct early endosome subpopulations. *Traffic* 15:1366–1389.
61. Luzio JP, Parkinson MDJ, Gray SR, Bright NA (2009) The delivery of endocytosed cargo to lysosomes. *Biochem Soc Trans* 37:1019–1021.
62. Bright NA, Wartosch L, Luzio JP (2015) Lysosome fusion in cultured mammalian cells. *Methods Cell Biol* 126:101–118.
63. D'Agostino M, Risselada HJ, Lürick A, Ungermann C, Mayer A (2017) A tethering complex drives the terminal stage of SNARE-dependent membrane fusion. *Nature* 551:634–638.
64. Huotari J, Helenius A (2011) Endosome maturation. *EMBO J* 30:3481–3500.
65. Falcón-Pérez JM, Nazarian R, Sabatti C, Dell'Angelica EC (2005) Distribution and dynamics of Lamp1-containing endocytic organelles in fibroblasts deficient in BLOC-3. *J Cell Sci* 118:5243–5255.
66. Wang S, Sun H, Tanowitz M, Liang XH, Crooke ST (2017) Intra-endosomal trafficking mediated by lysobisphosphatidic acid contributes to intracellular release of phosphorothioate-modified antisense oligonucleotides. *Nucleic Acids Res* 45: 5309–5322.
67. Jefferies HBJ, et al. (2008) A selective PIKfyve inhibitor blocks PtdIns(3,5)P(2) production and disrupts endomembrane transport and retroviral budding. *EMBO Rep* 9: 164–170.
68. Balderhaar HJ, Ungermann C (2013) CORVET and HOPS tethering complexes–Coordinators of endosome and lysosome fusion. *J Cell Sci* 126:1307–1316.
69. Lukinavičius G, et al. (2013) A near-infrared fluorophore for live-cell super-resolution microscopy of cellular proteins. *Nat Chem* 5:132–139.
70. Savina A, Furlán M, Vidal M, Colombo MI (2003) Exosome release is regulated by a calcium-dependent mechanism in K562 cells. *J Biol Chem* 278:20083–20090.
71. Willem J, ter Beest M, Scherphof G, Hoekstra D (1990) A non-exchangeable fluorescent phospholipid analog as a membrane traffic marker of the endocytic pathway. *Eur J Cell Biol* 53:173–184.
72. Vidal M, Mangeat P, Hoekstra D (1997) Aggregation reroutes molecules from a recycling to a vesicle-mediated secretion pathway during reticulocyte maturation. *J Cell Sci* 110:1867–1877.
73. Savina A, Vidal M, Colombo MI (2002) The exosome pathway in K562 cells is regulated by Rab11. *J Cell Sci* 115:2505–2515.
74. Bhatnagar S, Schorey JS (2007) Exosomes released from infected macrophages contain *Mycobacterium avium* glycopeptidolipids and are proinflammatory. *J Biol Chem* 282:25779–25789.
75. Futaki S, Nakase I (2017) Cell-surface interactions on arginine-rich cell-penetrating peptides allow for multiplex modes of internalization. *Acc Chem Res* 50:2449–2456.
76. Madani F, Lindberg S, Langel U, Futaki S, Gräslund A (2011) Mechanisms of cellular uptake of cell-penetrating peptides. *J Biophys* 2011:414729.
77. Erazo-Oliveras A, Muthukrishnan N, Baker R, Wang TY, Pellois JP (2012) Improving the endosomal escape of cell-penetrating peptides and their cargos: Strategies and challenges. *Pharmaceuticals (Basel)* 5:1177–1209.
78. Brock R (2014) The uptake of arginine-rich cell-penetrating peptides: Putting the puzzle together. *Bioconjug Chem* 25:863–868.
79. van den Berg A, Dowdy SF (2011) Protein transduction domain delivery of therapeutic macromolecules. *Curr Opin Biotechnol* 22:888–893.
80. Bechara C, Sagan S (2013) Cell-penetrating peptides: 20 years later, where do we stand? *FEBS Lett* 587:1693–1702.
81. Wender PA, Galliher WC, Goun EA, Jones LR, Pillow TH (2008) The design of guanidinium-rich transporters and their internalization mechanisms. *Adv Drug Deliv Rev* 60:452–472.
82. Rabideau AE, Pentelute BL (2016) Delivery of non-native cargo into mammalian cells using anthrax lethal toxin. *ACS Chem Biol* 11:1490–1501.
83. Peraro L, Kritzer JA (2018) Emerging methods and design principles for cell-penetrant peptides. *Angew Chem Int Ed Engl* 57:11868–11881.
84. Kalafatovic D, Giralt E (2017) Cell-penetrating peptides: Design strategies beyond primary structure and amphipathicity. *Molecules* 22:1929.
85. Thompson DB, Cronican JJ, Liu DR (2012) Engineering and identifying supercharged proteins for macromolecule delivery into mammalian cells. *Methods Enzymol* 503: 293–319.
86. Daniels DS, Schepartz A (2007) Intrinsically cell-permeable miniature proteins based on a minimal cationic PPII motif. *J Am Chem Soc* 129:14578–14579.
87. Smith BA, et al. (2008) Minimally cationic cell-permeable miniature proteins via alpha-helical arginine display. *J Am Chem Soc* 130:2948–2949.
88. Rink J, Ghigo E, Kalaidzidis Y, Zerial M (2005) Rab conversion as a mechanism of progression from early to late endosomes. *Cell* 122:735–749.
89. Millet JK, Whittaker GR (2018) Physiological and molecular triggers for SARS-CoV membrane fusion and entry into host cells. *Virology* 517:3–8.
90. Burkard C, et al. (2014) Coronavirus cell entry occurs through the endo-/lysosomal pathway in a proteolysis-dependent manner. *PLoS Pathog* 10:e1004502.
91. Carette JE, et al. (2011) Ebola virus entry requires the cholesterol transporter Niemann-Pick C1. *Nature* 477:340–343.
92. Li B, et al. (2017) The FgVps39-FgVam7-FgSso1 complex mediates vesicle trafficking and is important for the development and virulence of *Fusarium graminearum*. *Mol Plant Microbe Interact* 30:410–422.
93. Palmer GE, Cashmore A, Sturtevant J (2003) *Candida albicans* VPS11 is required for vacuole biogenesis and germ tube formation. *Eukaryot Cell* 2:411–421.
94. Liu X, Hu G, Panepinto J, Williamson PR (2006) Role of a VPS41 homologue in starvation response, intracellular survival and virulence of *Cryptococcus neoformans*. *Mol Microbiol* 61:1132–1146.
95. Geissenhöner A, Sievers N, Brock M, Fischer R (2001) *Aspergillus nidulans* DigA, a potential homolog of *Saccharomyces cerevisiae* Pep3 (Vps18), is required for nuclear migration, mitochondrial morphology and polarized growth. *Mol Genet Genomics* 266:672–685.
96. Mattie S, McNally EK, Karim MA, Vali H, Brett CL (2017) How and why intralumenal membrane fragments form during vacuolar lysosome fusion. *Mol Biol Cell* 28: 309–321.
97. Kweon DH, Kong B, Shin YK (2017) Hemifusion in synaptic vesicle cycle. *Front Mol Neurosci* 10:65.